Study of Subcooled Film Boiling on a Horizontal Disc: Part I—Analysis[1]

D. Banerjee

V. K. Dhir

Mechanical and Aerospace Engineering Department, University of California, Los Angeles, Los Angeles, CA 90095

In this work subcooled film boiling on a horizontal disc was studied analytically/numerically. Linearized stability analysis of a vapor film underlying a pool of heavier liquid was performed in three-dimensional, cylindrical coordinates. From the analysis the dominant wavelength and configuration of vapor releasing nodes was identified. Complete numerical simulation of the nonlinearly evolving interface have been carried out in axisymmetric coordinates. Finite difference method was used to simultaneously solve the equations governing conservation of mass, momentum, and energy in the vapor and liquid phases. The equations for the two phases were coupled through the matching of normal and tangential stresses and continuity of mass and energy at the interface. Second order projection method was employed for decoupling velocities from pressure. Numerical grid generation method was utilized to construct a grid system which was aligned with the interface. From the simulations the shape of the nonlinearly evolving interface, the growth rate of the interface, the flow and temperature fields in the vapor and liquid, and rate of heat transfer from the wall and into the subcooled liquid have been determined.
[DOI: 10.1115/1.1345889]

Keywords: Boiling; Film; Heat Transfer; Phase Change; Two-Phase

1 Introduction

The study of subcooled film boiling has significant applications in space vehicle and other systems operating in micro-gravity, thermal issues in high speed civil transport, heat treatment of metals, nuclear reactor design, cryogenic cooling for superconducting applications, and thermal storage systems among others.

Although film boiling has been studied extensively in the past, only a limited number of investigations have been performed for saturated and subcooled film boiling on horizontal surfaces. Berenson [1] used two-dimensional Taylor instability to obtain an expression for the saturated film boiling heat transfer coefficient on a horizontal surface. Berenson [1] proposed a static bubble model where he assumed that the vapor bubbles were arranged on a square grid with spacing equal to the ''most dangerous wavelength'' (λ_{d2}) obtained from two-dimensional analysis of Taylor instability.

Hosler and Westwater [2] experimentally investigated saturated film boiling of water and Freon-11 on a horizontal surface and found the heat transfer data to show a large variability. However, the mean data tended to show a good agreement with predictions from Berenson's model. More recently Ramilison and Lienhard [3] reproduced Berenson's experiments and obtained film and transition boiling data by controlling the temperature of the horizontal disc. They found that transition film boiling data for Freon-113, acetone, benzene and *n*-pentane deviated from the prediction from Berenson's semi-empirical model and the magnitude of deviations depended on the surface condition. Klimenko and Shelepen [4] have developed a generalized correlation for saturated film boiling on a horizontal surface.

Very recently Son and Dhir [5] performed a complete numerical simulation of saturated film boiling on a horizontal surface. They carried out an axisymmetric analysis of the region surrounding the bubble releasing nodes. From the analysis it was shown that heat transfer coefficients vary strongly both spatially and temporally. The predicted bubble diameter at departure and height were found to be in agreement with the reported data but area and time averaged heat transfer coefficients were about 34 percent lower than those obtained from Berenson's model. The discrepency was attributed to the presence of three dimensional effects which were not considered in the numerical simulations.

Hamill and Baumeister [6] performed a theoretical analysis of subcooled film boiling on a horizontal plate. Based on the maximum entropy generation rate postulate and by assuming a static and empirical configuration for the vapor bubbles, they arrived at an estimate for the film boiling heat transfer coefficients in subcooled film boiling. The authors superimposed the contribution of radiation heat transfer and convection in the subcooled liquid on the film boiling heat transfer coefficient for saturated liquid as

$$\bar{h} = \bar{h}_o + 0.88\bar{h}_r + 0.12\bar{h}_{nc}\frac{\Delta T_{\text{sub}}}{\Delta T_W}, \tag{1}$$

where, $\bar{h}_o$ is the saturation film boiling heat transfer coefficient, and $\bar{h}_r$ and $\bar{h}_{nc}$ are the radiation and convection heat transfer coefficients, respectively. However, no experimental data were provided in support of the analysis.

Linearized analysis of two dimensional Taylor instability has been performed by several investigators. Dhir and Lienhard [7] extended Bellman and Pennington's [8] analysis to include the combined effect of fluid viscosity and radial curvature of a cylinderical interface to obtain the ''most dangerous'' wave length and the corresponding growth rate. Sernas et al. [9] were the first to suggest for film boiling a three-dimensional Taylor wave pattern in cartesian coordinates. This wave pattern eliminated the conceptual difficulties that existed in wave patterns based on two-dimensional analysis. Jacobs [10] studied Taylor instability in a circular geometry in which a liquid column formed in a circular pipe was accelerated downward in air. Jacobs also performed weakly nonlinear analysis of the three-dimensional Taylor instability. The analysis involved small perturbation expansions about the critical wavenumber (corresponding to zero growth rate). Predictions of shapes of the non-linear instabilities from this method were found to match the experimentally observed shapes during the initial part of the growth of the instability. The growth rates predicted from linear theory were found to be valid much later in time than the weakly non-linear analysis. The analyses also

[1]This work received support from the National Science Foundation.

Contributed by the Heat Transfer Division for publication in the JOURNAL OF HEAT TRANSFER. Manuscript received by the Heat Transfer Division January 20, 2000; revision received October 31, 2000. Associate Editor: V. Carey.

showed that the axisymmetric instabilities (e.g., circular and hexagonal) grow much faster compared to other geometries (e.g., square, rectangular, etc.). However, the axisymmetric solutions did not converge to the Cartesian coordinate solutions, for radial wave numbers approaching infinity, because of the nature of the coefficients of the governing equations.

In this study linear three-dimensional analysis of Taylor instability has been performed in cylindrical coordinates with the objective of predicting the configuration of wave crests on a circular disc. The motivation for such a study is to evaluate the pattern of vapor bubbles under pool boiling conditions for film boiling on a horizontal flat disk. The vapor bubble pattern identified from the linear analysis of three-dimensional Taylor instability is utilized for numerical simulation of non-linear evolution of the interface in subcooled film boiling.

2 Analysis

2.1 Linear Three-Dimensional Taylor Instability Analysis. The instability at the interface of a lighter fluid underlying a heavier fluid has been modeled in this study, where the acceleration due to gravity is directed from the heavier to the lighter fluid. Under the assumptions that the fluids are inviscid and incompressible, the fluid layers are of infinite depth, and the nonlinear terms are small, the linearized governing equations for both fluids, expressed in cylindrical coordinates are as follows:

Continuity Equation

$$\frac{1}{r}\frac{\partial(ru)}{\partial r}+\frac{1}{r}\frac{\partial w}{\partial \theta}+\frac{\partial v}{\partial y}=0 \tag{2}$$

Momentum Equation

$$\rho\frac{\partial u}{\partial t}=-\frac{\partial p}{\partial r} \tag{3}$$

$$\rho\frac{\partial w}{\partial t}=-\frac{1}{r}\frac{\partial p}{\partial \theta} \tag{4}$$

$$\rho\frac{\partial v}{\partial t}=-\frac{\partial p}{\partial y}-\rho g, \tag{5}$$

where u, w, and v are the radial, polar and vertical components of the velocity vector $\vec{\mathbf{u}}$. In terms of the potential function ϕ, the velocity can be written as

$$\vec{\mathbf{u}}=\nabla\phi=u\hat{\mathbf{r}}+w\hat{\theta}+v\hat{\mathbf{y}}, \tag{6}$$

where $\hat{\mathbf{r}}$, $\hat{\theta}$, $\hat{\mathbf{y}}$ are the unit vectors in the radial, angular and vertical direction in cylindrical polar coordinates and ∇ is the gradient operator. Substituting Eq. (6) in the continuity equation (Eq. (2)) we obtain,

$$\nabla^2\phi=\frac{1}{r}\frac{\partial}{\partial r}\left(r\frac{\partial\phi}{\partial r}\right)+\frac{1}{r^2}\frac{\partial^2\phi}{\partial\theta^2}+\frac{\partial^2\phi}{\partial y^2}=0. \tag{7}$$

The solution of the above equation is given by

$$\phi(r,\theta,y,t)=C_{mn}J_m(k_nr)\cos(m\theta)e^{(-k_ny)}e^{(-i\omega_nt)}, \tag{8}$$

where J_m is the Bessel function of the first kind of order m. Here m and n denote the eigenvalues of Eq. (7), while k_n denotes the wavenumber corresponding to mode number n. The shape of the perturbed interface is assumed to be

$$\overline{\eta}(r,\theta,t)=\overline{\eta}_oJ_m(k_nr)\cos(m\theta)e^{(-i\omega_nt)}, \tag{9}$$

where $\overline{\eta}_o$ is the initial amplitude of the interfacial disturbance and ω_n denotes the growth rate (It should be noted that $m=0$ corresponds to the two-dimensional case).

The kinematic condition at the interface yields

$$v\big|_{\overline{\eta}}=\frac{\partial\overline{\eta}}{\partial t}+(\vec{u}\cdot\nabla)v. \tag{10}$$

Substituting Eqs. (6), (8), and (9) in the above equation after neglecting the nonlinear terms (the last term on the right in the above equation), the following relation is obtained:

$$C_{mn}=\frac{i\overline{\eta}_o\omega_n}{k_n}. \tag{11}$$

Since the Taylor instability during film boiling results in a standing wave, above a wave crest at $r=r_n$ we can impose $u\big|_{\overline{\eta}}=0$. Hence from Eqs. (6) and (8) we also get the relation:

$$\frac{\partial}{\partial r}J_m(k_nr)\big|_{r=r_n}=0 \tag{12}$$

$$k_n=\alpha_{mn}/r_n, \tag{13}$$

where α_{mn} is the n^{th} root of Eq. (12) and r_n is the radius of the concentric ring number n of the wave crests. The values of α_{mn} can be obtained from a standard handbook of mathematical functions. The same relationship was used by Daly [11] for numerical simulation of two-dimensional Taylor instability in cylindrical coordinates. However, this would suggest that the values of wavenumber approach zero for an infinite size heater, which is conceptually erroneous. This paradox will be resolved as we solve the dispersion relation.

Dispersion Relation. Substituting Eq. (6) in Eq. (5) and integrating in the y direction from 0 to $\overline{\eta}$ the solution for the pressure $p\big|_{\overline{\eta}}$ at $y=\overline{\eta}$ is obtained as

$$p\big|_{\overline{\eta}}=p_o-\rho g\,\eta+\rho\frac{\partial\phi}{\partial t}, \tag{14}$$

where p_o is the mean pressure at the interface in the unperturbed condition.

Using the relation

$$p_v-p_l=\gamma/R_s \tag{15}$$

and Eqs. (8), (11), and (14) for liquid and vapor we get

$$(\rho_l+\rho_v)\frac{\omega_n^2\overline{\eta}}{k_n}=\frac{\gamma}{R_s}-(\rho_l-\rho_v)g\,\overline{\eta}, \tag{16}$$

where R_s is the radius of curvature of the interface. An expression for R_s is obtained as (see Daly [11]):

$$\frac{1}{R_s}=\frac{1}{R_1}+\frac{1}{R_2};\quad \frac{1}{R_1}=\left|\frac{\partial^2\overline{\eta}}{\partial r^2}\right|;\quad \frac{1}{R_2}=\left|\frac{1}{r}\frac{\partial\overline{\eta}}{\partial r}\right|. \tag{17}$$

Substituting Eq. (9) in the Eq. (16), the dispersion relation is obtained as

$$\omega_{n_i}^2=\frac{-\gamma k_n^3\left|-1+\dfrac{m^2}{4k_n^2r^2}\right|+(\rho_l-\rho_v)gk_n}{(\rho_l+\rho_v)}, \tag{18}$$

where ω_{n_i} is the imaginary component of ω_n. Using the characteristic length l_o and characteristic growth rate ω_o defined as

$$l_o=\left[\frac{\gamma}{(\rho_l-\rho_v)g}\right]^{1/2};\quad \omega_o=\left[\left(\frac{\rho_l-\rho_v}{\rho_l+\rho_v}\right)\left(\frac{g}{l_o}\right)\right]^{1/2} \tag{19}$$

the dispersion relation Eq. (18) is obtained in dimensionless form as

$$\left(\frac{\omega_{n_i}^2}{\omega_o^2}\right)=(k_nl_o)\left[-(k_nl_o)^2\left|-1+\frac{m^2}{4k_n^2r^2}\right|+1\right]. \tag{20}$$

The characteristic length, l_o is obtained by balancing surface tension and buoyancy forces, whereas the chacteristic frequency, w_o,

is representative of the growth rate of Taylor instability of the interface between two inviscid fluid layers of infinite extent.

Three cases are possible from terms within the absolute-value sign:

Case 1: $m^2 > 4k_n^2 r^2$

$$\left(\frac{\omega_{n_i}^2}{\omega_o^2}\right) = (k_n l_o)\left[(k_n l_o)^2 - \left\{\left(\frac{m}{2r/l_o}\right)^2 - 1\right\}\right] \tag{21}$$

Case 2: $m^2 = 4k_n^2 r^2$

$$\left(\frac{\omega_{n_i}^2}{\omega_o^2}\right) = k_n l_o \tag{22}$$

Case 3: $m^2 < 4k_n^2 r^2$

$$\left(\frac{\omega_{n_i}^2}{\omega_o^2}\right) = (k_n l_o)\left[-(k_n l_o)^2 + \left\{\left(\frac{m}{2r/l_o}\right)^2 + 1\right\}\right] \tag{23}$$

Critical Wavelength. For each of the three possible dispersion relationships, the critical wavelength corresponding to zero growth rate can be obtained by setting $\omega_{n_i} = 0$ in Eqs. (21), (22), and (23). For purposes of clarity a characteristic radius is obtained as $r_o = m/2k_{n_c}$ where k_{n_c} is obtained from the dispersion relations as follows:

Case 1: $m^2 > 4k_n^2 r^2$ (or $r < r_o$):

$$k_{n_c} = \frac{1}{l_o}\left[\left(\frac{m}{2r/l_o}\right)^2 - 1\right]^{1/2} \tag{24}$$

Case 2: $m^2 = 4k_n^2 r^2$ (or $r = r_o$):

$$k_{n_c} = 0 \tag{25}$$

Case 3: $m^2 < 4k_n^2 r^2$ (or $r > r_o$):

$$k_{n_c} = \frac{1}{l_o}\left[\left(\frac{m}{2r/l_o}\right)^2 + 1\right]^{1/2} \tag{26}$$

It should be noted that for Case 1 and Case 3 the relationship between ''most dangerous wavenumber'' or k_{n_d} (corresponding to maximum growth rate) and the critical wavenumber, k_{n_c} is given by

$$k_{n_d} = k_{n_c}/\sqrt{3}, \tag{27}$$

which is the same as in two-dimensional analyses in Cartesian coordinates (Bellman and Pennington [8]) and is also the same in three-dimensional analyses in Cartesian coordinates (Sernas et al., [9]). For Case 2, since $k_{n_c} = 0$ this is valid only for $m = 0$. Thus this is same as two-dimensional configuration and hence we obtain the same relation as Eq. (27), though here we arrive at the solution $k_{n_d} = k_{n_c}/\sqrt{(3)} = 0$.

Case 2 yields a trivial solution, which is not relevant to the present case. Also, from Case 1 the values of k_n obtained are not of significance in the situation analyzed here since these values of k_n occur before the first ring of crests. Hence, Cases 1 and 2 are not of interest.

Case 3 yields the only viable solution to k_n. Equation (26) implies that as the radius of the heater approaches infinity, the critical wavenumber approaches the value obtained from analyses performed in Cartesian coordinates. Hence, this resolves the paradox mentioned earlier.

2.2 Numerical Analysis Of Nonlinear Growth of the Interface. Numerical simulations of the evolution of the vapor liquid interface during subcooled film were carried out by assuming that the process could be considered to be axisymmetric. In carrying out the analysis the wall temperature was specified and was assumed to remain constant during the evolution of the interface. The thermophysical properties of the vapor were evaluated at the mean of the wall and interface temperatures. Similarly the liquid properties were calculated at the mean temperature between interface and the pool. Radiation contribution was neglected under the assumption that wall temperatures were not high enough for heat loss by radiation to be significant. In dimensionless form the equations governing the conservation of mass, momentum, and energy are written for vapor and liquid, respectively, as follows:

$$\frac{\partial(ru_v)}{\partial r} + \frac{\partial(rv_v)}{\partial y} = 0 \tag{28}$$

$$\frac{Du_v}{Dt} = -\frac{\partial p_v}{\partial r} + \frac{1}{\mathrm{Re}_v}\left(\nabla^2 u_v - \frac{u_v}{r^2}\right) \tag{29}$$

$$\frac{Dv_v}{Dt} = -\frac{\partial p_v}{\partial y} + \frac{1}{\mathrm{Re}_v}\nabla^2 v_v \tag{30}$$

$$\frac{D\theta_v}{Dt} = \frac{1}{\mathrm{Pr}_v\,\mathrm{Re}_v}\nabla^2\theta_v \tag{31}$$

$$\frac{\partial(ru_l)}{\partial r} + \frac{\partial(rv_l)}{\partial y} = 0 \tag{32}$$

$$\frac{Du_l}{Dt} = -\frac{\partial p_l}{\partial r} + \frac{\hat{\rho}}{\hat{\mu}}\frac{1}{\mathrm{Re}_v}\left(\nabla^2 u_l - \frac{u_l}{r^2}\right) \tag{33}$$

$$\frac{Dv_l}{Dt} = -\frac{\partial p_l}{\partial y} + \frac{\hat{\rho}}{\hat{\mu}}\frac{1}{\mathrm{Re}_v}\nabla^2 v_l + \frac{\hat{\rho}}{\hat{\alpha}\hat{\mu}}\frac{\mathrm{Ra}_l}{\mathrm{Pr}_v\,\mathrm{Re}_v^2}\theta_l \tag{34}$$

$$\frac{D\theta_l}{Dt} = \frac{1}{\hat{\alpha}}\frac{1}{\mathrm{Pr}_v\,\mathrm{Re}_v}\nabla^2\theta_l, \tag{35}$$

where for general dependent variable, ϕ, which represents dependent variables, u, v, and θ,

$$\frac{D\phi}{Dt} = \frac{\partial\phi}{\partial t} + u\frac{\partial\phi}{\partial r} + v\frac{\partial\phi}{\partial y} \tag{36}$$

$$\nabla^2\phi = \frac{1}{r}\frac{\partial}{\partial r}\left(\frac{\partial\phi}{\partial r}\right) + \frac{\partial^2\phi}{\partial y^2} \tag{37}$$

also

$$\mathrm{Re}_v = \frac{\rho_o u_o l_o}{\mu_v}; \quad \mathrm{Pr}_v = \frac{\nu_v}{\alpha_v}; \quad \mathrm{Ra}_l = \frac{g\beta_l(T_{\mathrm{sat}} - T_\infty)l_0^3}{\nu_l\alpha_l};$$

$$\hat{\rho} = \frac{\rho_v}{\rho_l}; \quad \hat{\mu} = \frac{\mu_v}{\mu_l}; \quad \hat{\alpha} = \frac{\alpha_v}{\alpha_l}.$$

In carrying out numerical simulation the characteristic length, l_o, and characteristic growth rate frequency ω_o are defined in Eq. (19). The characteristic time, t_o, characteristic velocity, u_o, and ''most dangerous frequency'' ω_d are defined as

$$t_o = \sqrt{\frac{l_o}{g}}; \quad u_o = \frac{l_o}{t_o}; \quad \omega_d = 0.62 \times \omega_o. \tag{38}$$

The characteristic time, t_o, is obtained by combining the gravitational acceleration and the characteristic length, whereas the characteristic velocity, u_o, is obtained by combining characteristic length and characteristic time.

The dimensionless temperatures are defined as

$$\theta_v = \frac{T_v - T_{\mathrm{sat}}}{\Delta T_w}; \quad \theta_l = \frac{T_l - T_\infty}{\Delta T_{\mathrm{sub}}}, \tag{39}$$

where T_v and T_l denote the vapor and liquid temperature variables, respectively. The dimensionless pressures are defined as

$$p_v = \frac{p_v^* + \rho_v g y}{\rho_v u_o^2}; \quad p_l = \frac{p_l^* + \rho_l g y}{\rho_l u_o^2}, \tag{40}$$

and p_v^* and p_l^* denote the static pressures, respectively. It is to be noted that p is defined as a pressure whose gradient is subtracted by a gravitational head which otherwise would appear in momentum equations. Also, the degree of superheat ΔT_w and degree of subcooling ΔT_{sub} are defined as

$$\Delta T_w = T_{\text{wall}} - T_{\text{sat}}; \quad \Delta T_{\text{sub}} = T_{\text{sat}} - T_\infty,$$

where, T_{sat} is the saturation temperature of the test fluid and T_∞ is the temperature of the liquid phase far away from the vapor-liquid interface.

For complex geometries, the solution procedure of governing equations are simplified by transformation to generalized, nonorthogonal, curvilinear coorodinates. This provides flexibility in improving resolution in desired regions of the domain of solution. Since two-phase flow with a complex interface is difficult to solve in (x, y) coordinates, the following coordinate transformation is used:

$$\xi = \xi(x,y,t); \quad \eta = \eta(x,y,t). \tag{41}$$

When the interface is deformed largely, interior grid points are difficult to determine algebraically. As such a grid system aligned with a complex interface is generated numerically by solving Poisson's equations (Thompson et al. [12]).

At the interface, $\theta_v = 0$ or $T_v = T_{\text{sat}}$ and $\theta_l = 1$ or $T_l = T_{\text{sat}}$. At the rigid wall

$$u_v = 0; \quad v_v = 0 \tag{42}$$

$$T_v = T_{\text{wall}}, \tag{43}$$

where, T_{wall} is the wall temperature. At the locations of symmetry with respect to y-axis and the centerline

$$u_v = 0; \quad \frac{\partial v_v}{\partial r} = 0$$

$$u_l = 0; \quad \frac{\partial v_l}{\partial r} = 0 \tag{44}$$

$$\frac{\partial \theta_v}{\partial r} = 0 \tag{45}$$

$$\frac{\partial \theta_l}{\partial r} = 0. \tag{46}$$

Far away from the interface

$$\frac{\partial u_l}{\partial r} = 0; \quad \frac{\partial v_l}{\partial y} = 0; \quad \theta_l = 0. \tag{47}$$

At the interface, the matching conditions for velocities and stresses are (see, e.g., Shyy [13]):

$$u_l - u_v = (1-\hat{\rho}) \frac{y_\xi \dot{m}}{\sqrt{x_\xi^2 + y_\xi^2}}$$

$$v_l - v_v = -(1-\hat{\rho}) \frac{x_\xi \dot{m}}{\sqrt{x_\xi^2 + y_\xi^2}}. \tag{48}$$

For shear stress and pressure

$$\frac{1}{\hat{\mu}} \tau_l - \tau_v = 0 \tag{49}$$

$$\frac{1}{\hat{\rho}} p_l - p_v = \frac{2}{\text{Re}_v} \left(\frac{1}{\mu} \sigma_l - \sigma_v \right) + (1-\hat{\rho}) \frac{\dot{m}^2}{r^2 (x_\xi^2 + y_\xi^2)} + \frac{(1-\hat{\rho})}{\hat{\rho}} (y - y_o) - \frac{(1-\hat{\rho})}{\hat{\rho}} \frac{1}{R_s}. \tag{50}$$

In the above equations

$$\dot{m} = \frac{\text{Ja}_v}{\text{Pr}_v \, \text{Re}_v} \frac{r(x_\xi^2 + y_\xi^2)}{J} \left(\theta_{v\eta} - \frac{\overset{*}{Ja}_l}{\overset{*}{Ja}_v} \frac{\hat{\alpha}}{\hat{\rho}} \theta_{l\eta} \right) \tag{51}$$

$$J_{a_v}^* = \frac{C_{p_v} \Delta T_w}{h_{fg}} \tag{52}$$

$$\overset{*}{Ja}_l = \frac{C_{p_l} \Delta T_{\text{sub}}}{h_{fg}} \tag{53}$$

$$\sqrt{x_\xi^2 + y_\xi^2}\, \tau = \frac{x_\xi^2 + y_\xi^2}{J} \overline{u}_\eta - \frac{x_\xi x_\eta + y_\xi y_\eta}{J} \overline{u}_\xi + \frac{x_\xi u_\xi - y_\xi u_\xi}{\sqrt{x_\xi^2 + y_\xi^2}} - \frac{x_\xi^2 + y_\xi^2}{J} \left[\left(\frac{x_\xi}{\sqrt{x_\xi^2 + y_\xi^2}} \right)_\eta u + \left(\frac{y_\xi}{\sqrt{x_\xi^2 + y_\xi^2}} \right)_\eta v \right] + \frac{x_\xi x_\eta + y_\xi y_\eta}{J} \left[\left(\frac{x_\xi}{\sqrt{x_\xi^2 + y_\xi^2}} \right)_\xi u + \left(\frac{y_\xi}{\sqrt{x_\xi^2 + y_\xi^2}} \right)_\xi v \right] \tag{54}$$

$$\sigma = -c \frac{u}{r} - \frac{x_\xi u_\xi + y_\xi v_\xi}{x_\xi^2 + y_\xi^2}$$

$$\frac{1}{R_s} = -\frac{x_\xi y_{\xi\xi} - y_\xi x_{\xi\xi}}{(x_\xi^2 + y_\xi^2)^{3/2}} - c \frac{y_\xi}{r \sqrt{x_\xi^2 + y_\xi^2}}. \tag{55}$$

In carrying out the computations, the energy equation is solved prior to the momentum equations because initially only θ is unknown in Eqs. (31) and (35). In this study, the discretized equations are solved by an iterative method rather than by direct inversion of matrix. To enhance the rate of convergence of iterations, a relaxation factor obtained from orthogonal-residual method (Streett and Hussaini [14]) is used.

The numerical model employed in this study is similar to that given by Banerjee [15] and Son and Dhir [16]. For the details (about the discretization of the governing equations, coordinate transformation, numerical grid generation and solution procedure for contravariant velocity vectors employed in this study—using second order projection method and orthogonal residual method) the reader is referred to the above mentioned references.

An explicit scheme was used for marching in time. The time steps during computations were varied in the range 10^{-3} to 10^{-5} to satisfy the CFL (<1) condition for a grid size of 42×64 in the fluid region. The time step was varied, in accordance with the CFL condition, due to reduction in the minimum size of the nonuniform grid as the bubble evolved. The smallest grid dimension varied from 5×10^{-2} to $2 \times 10^{-3} l_o$. It took about 8–10 hours of CPU time on CRAY C90 to calculate one cycle of bubble evolution.

The numerical model was tested for its accuracy by comparing with the numerical results of Son [5] for saturated film boiling of water. The results were in agreement with the numerical predictions of Son [5]. The numerical method was also tested for its accuracy by comparing the predicted early growth rate of the interface with that determined from the linear instability theory for a two-dimensional interface. For a rigid adiabatic wall, the numerical error was found to be less than 1 percent. The sensitivity of the results to grid size was also tested. When the number of grid points was doubled the difference in the calculated Nusselt numbers based on area and time averaged heat transfer coefficients were in agreement with each other within 1 percent. As such, all of the results reported in this work were obtained with the number of grids noted earlier.

3 Results and Discussion

Before proceeding with the numerical simulation of an evolving interface, it is necessary to determine the computational domain. The extent of the computational domain depends on the dominant wavelength. As such we first discuss the results obtained from the dispersion relation, Eq. (26).

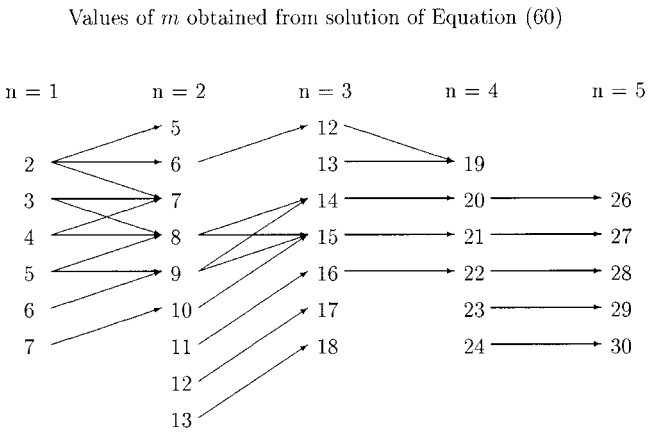

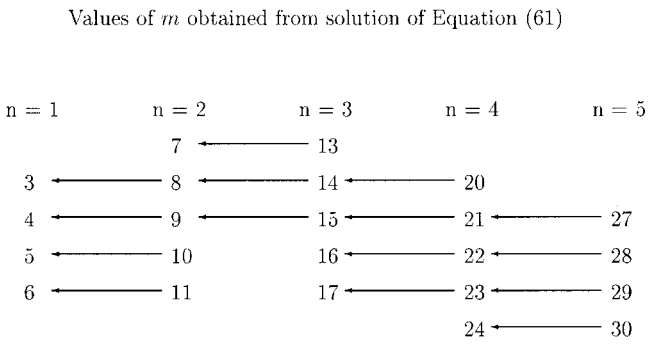

Fig. 1 Values of *m* obtained from solution of Eqs. (60) and (61) for spatial distribution of wave peaks corresponding to wave number k_{n_d} both in the radial and in the circumferential directions

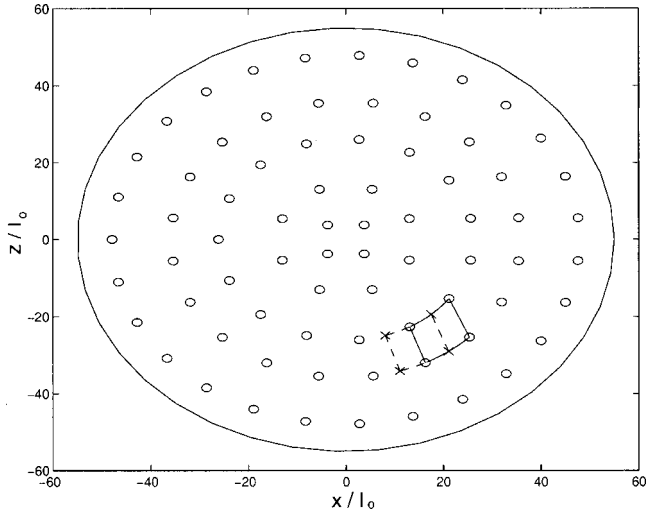

Fig. 2 Plot of crests of the three-dimensional Taylor wave on a circular plate for (*m*,*n*) values of (4, 1), (8, 2), (15, 3), (21, 4), and (27, 5). The circular plate, radial rings and wave crests are shown elliptical in the figure.

Table 1 Number of peaks supported by the region between consecutive rings

n	$n+1$	(Number of wave crests)/ λ_{d2}^2
1	2	0.8
2	3	1.1
3	4	1
4	5	0.98

3.1 Dominant Wavelength. The dispersion relation, Eq. (26) involves three unknowns, namely *m*, *n*, and *r*. Thus two additional relations are needed to determine the wavenumbers corresponding to critical or ''most dangerous'' wavelength. A second relation is provided by Eq. (13). Since in film boiling, no preference is expected to be given to perturbations that grow either in radial or azimuthal directions, we obtain the third relation by assuming that the dominant wavelength in the azimuthal direction is the same as in the radial direction:

$$r_{n+1}-r_n=\frac{2\pi r_n}{m}, \tag{56}$$

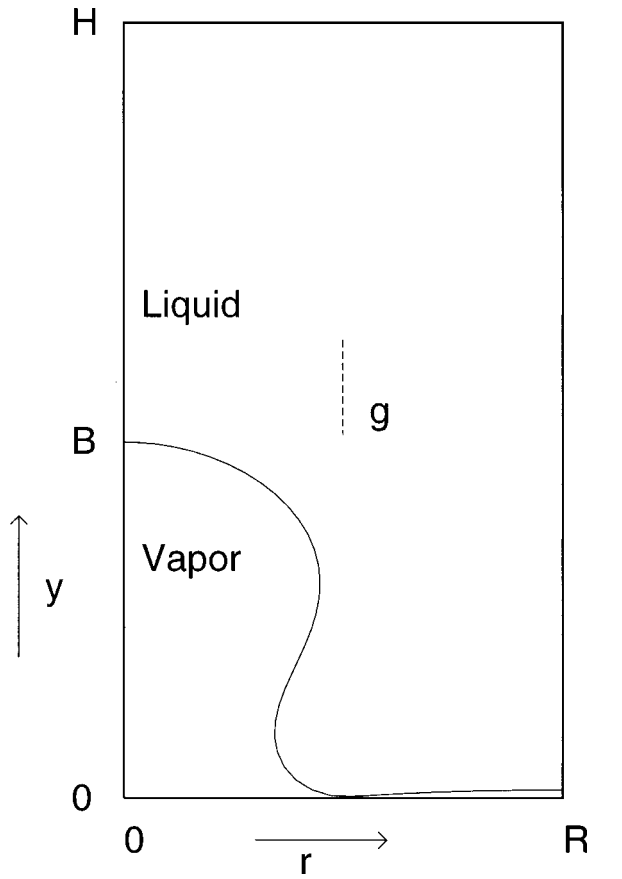

Fig. 3 Computational domain for solution of fluid side governing equations. In the computations *H* was set to 15, *R* was set to 4.34. The value of *B* changed as the height of the vapor bubble changed with time. The number of grids used in the vapor side was 42×22, with 42 grid points along the radial direction. The number of grids used in the liquid side was 42 ×42 in simulation runs for saturated film boiling and 42×77 in simulation runs for subcooled film boiling.

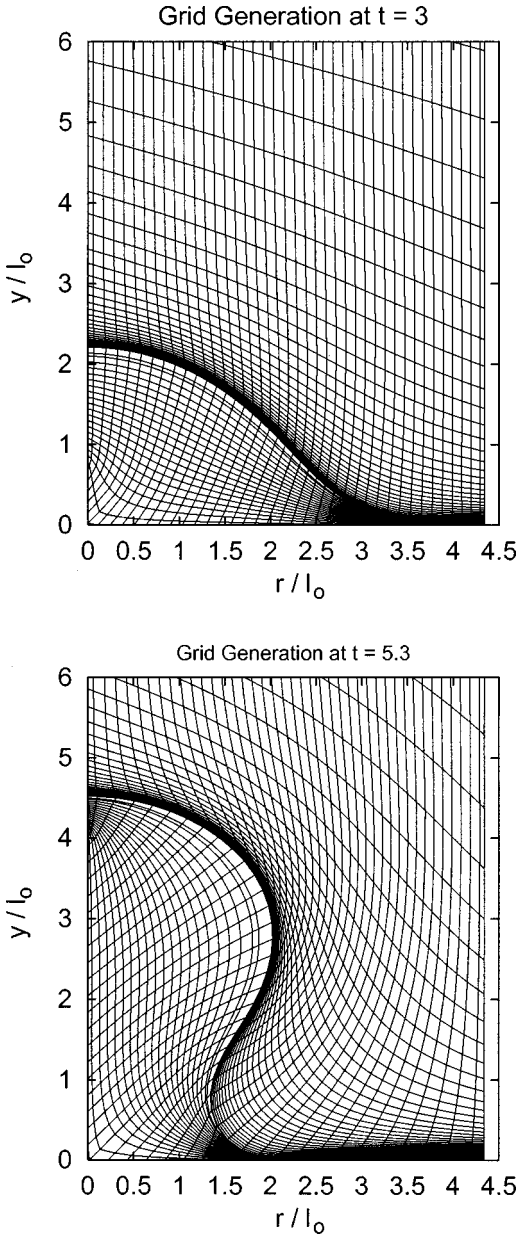

Fig. 4 Plot of grid locations for film boiling of saturated PF-5060 at $Ja_l^*=0.77$, and $Ja_v^*=0.133$, i.e., $\Delta T_W=100°C$, and $\Delta T_{sub}=10°C$. The radial and vertical distances are non-dimensionalized with respect to l_o. Time t is non-dimensionalized with respect to t_o.

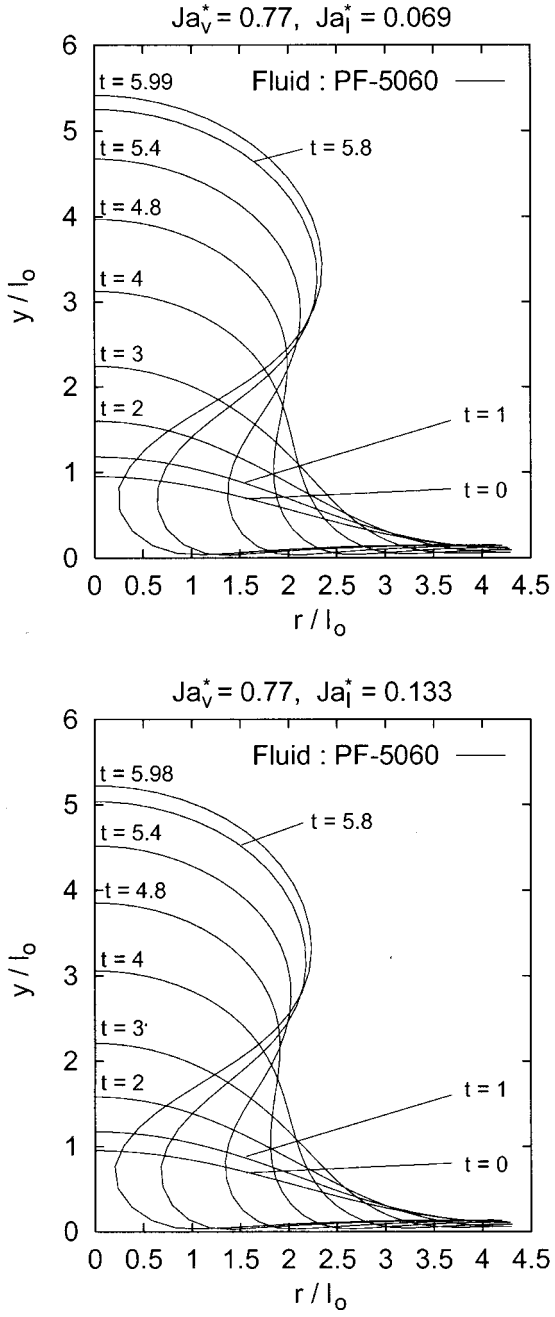

Fig. 5 Numerical predictions for temporal evolution of the liquid-vapor interface for wall superheat, $\Delta T_W=100°C$ and $\Delta T_{sub}=5°C$ and 10°C. The radial distances and interface heights are non-dimensionalized with respect to l_o. Time t is non-dimensionalized with respect to t_o.

where n and $n+1$ are the ring numbers of circumferential arrangement of wave peaks as we move radially out from the center. Similarly if one moves radially inwards, the relation becomes:

$$r_n - r_{n-1} = \frac{2\pi r_n}{m}. \tag{57}$$

Using Eq. (13) in Eqs. (56) and (57) the following relations are obtained, respectively:

$$\frac{\alpha_{m',n+1}}{k_{n+1}} - \frac{\alpha_{m,n}}{k_n} = \frac{2\pi}{m} \times \frac{\alpha_{m,n}}{k_n} \tag{58}$$

or,

$$\frac{\alpha_{m,n}}{k_n} - \frac{\alpha_{m',n-1}}{k_{n-1}} = \frac{2\pi}{m} \times \frac{\alpha_{m,n}}{k_n}, \tag{59}$$

where m' denotes the number of wave nodes at the preceeding or succeeding ring from ring n.

It can be shown from the dispersion relation Eq. (26) that the wavenumber k_n becomes independent of radius, r within a short distance from the origin. The asymptotic value of k_n is reached before the occurrence of the first concentric ring of the wave nodes. Hence in the above equations, it can be assumed that $k_{n+1}=k_n=k_{n-1}$. This enables a solution for m for a given n which is coupled with the solution of m' at ring number $n+1$ (or $n-1$). Therefore, we obtain from Eqs. (58) and (59), respectively, as follows:

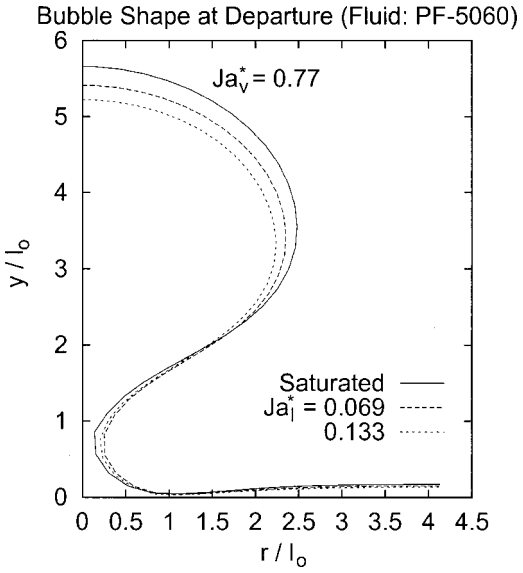

Fig. 6 Comparison of interface shape at bubble departure for wall superheat, ΔT_W=100°C, and liquid subcoolings, ΔT_{sub} =0°C, 5°C, and 10°C. The interface height and radius are non-dimensionalized with respect to l_o.

$$m = \frac{2\pi\alpha_{m,n}}{\alpha_{m',n+1} - \alpha_{m,n}} \tag{60}$$

or,

$$m = \frac{2\pi\alpha_{m,n}}{\alpha_{m,n} - \alpha_{m',n-1}}. \tag{61}$$

The above two equations describe implicit solutions for the *probable* values of m for a given n. Hence, either of the values of m obtained from the above equations are possible. This yields a set of solutions for (m, n) which provide a spatial distribution of wave peaks which are equidistant in the radial and circumferential directions.

Figure 1 shows the values of m for each ring number n obtained from Eqs. (60) and (61) assuming that the distance between the wave amplitude peaks (crests) correspond to the most dangerous wave number, k_{n_d}. In the figure, each column corresponds to the number of concentric ring. For example, when $n=1$, the minimum possible value of m is 2, according to Eq. (60). Hence, 2 is listed under first column for the solution of Eq. (60). When $m=2$ and $n=1$ the possible values of m for $n=2$ are 5, 6, and 7, according to Eq. (60). Hence arrows have been drawn in Fig. 1 from 2 in the first column pointing to 5, 6, and 7 in the second column. When $m=5$ and $n=2$ no solution is possible to Eq. (60) for values of m at $n=3$, so that the inter-crest separation distance

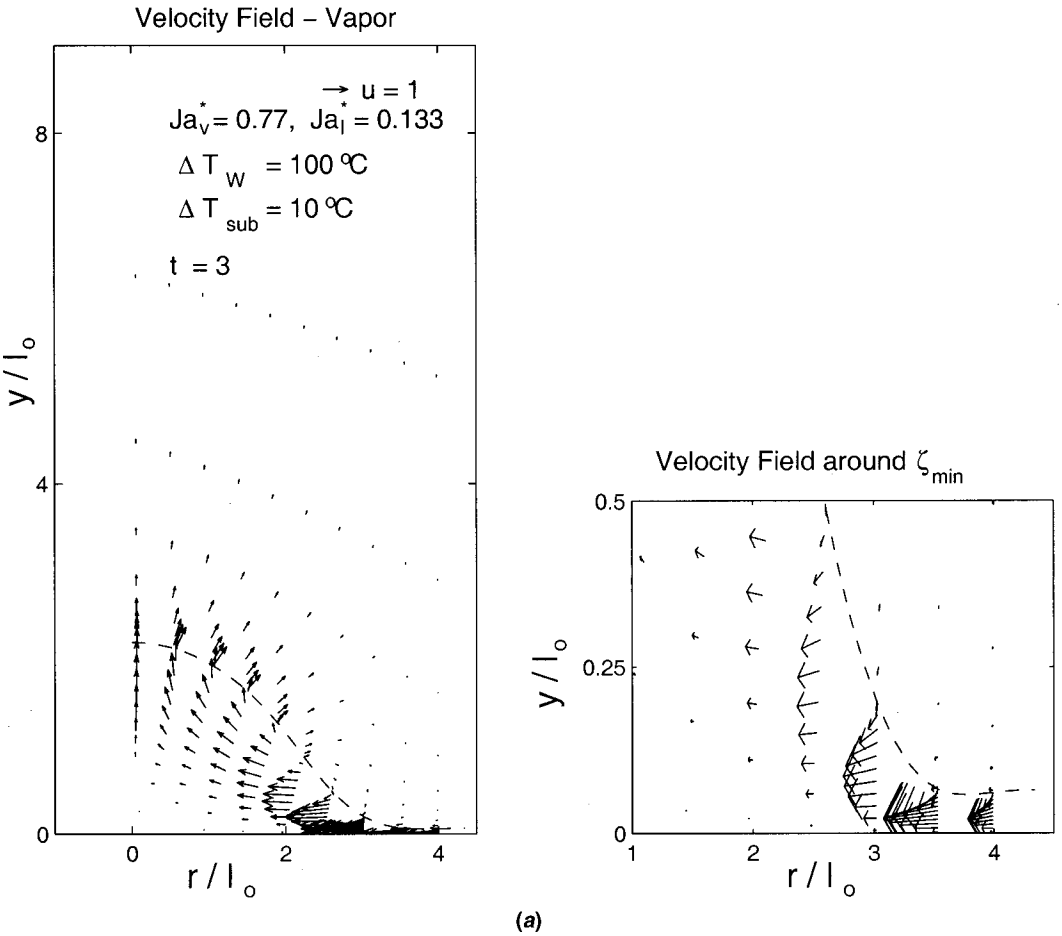

(*a*)

Fig. 7 (*a*) Spatial distribution of velocity vectors for ΔT_W=100°C, ΔT_{sub}=10°C and t=3. Time is non-dimensionalized with respect to t_o and velocity is non-dimensionalized with respect to u_o. The length of arrows plotted in the figure at the right are 2 times the respective length of arrows in the figure on the left; (*b*) spatial distribution of isotherms (θ) for ΔT_W=100°C and ΔT_{sub}=10°C at t=3. Time is non- dimensionalized with respect to t_o.

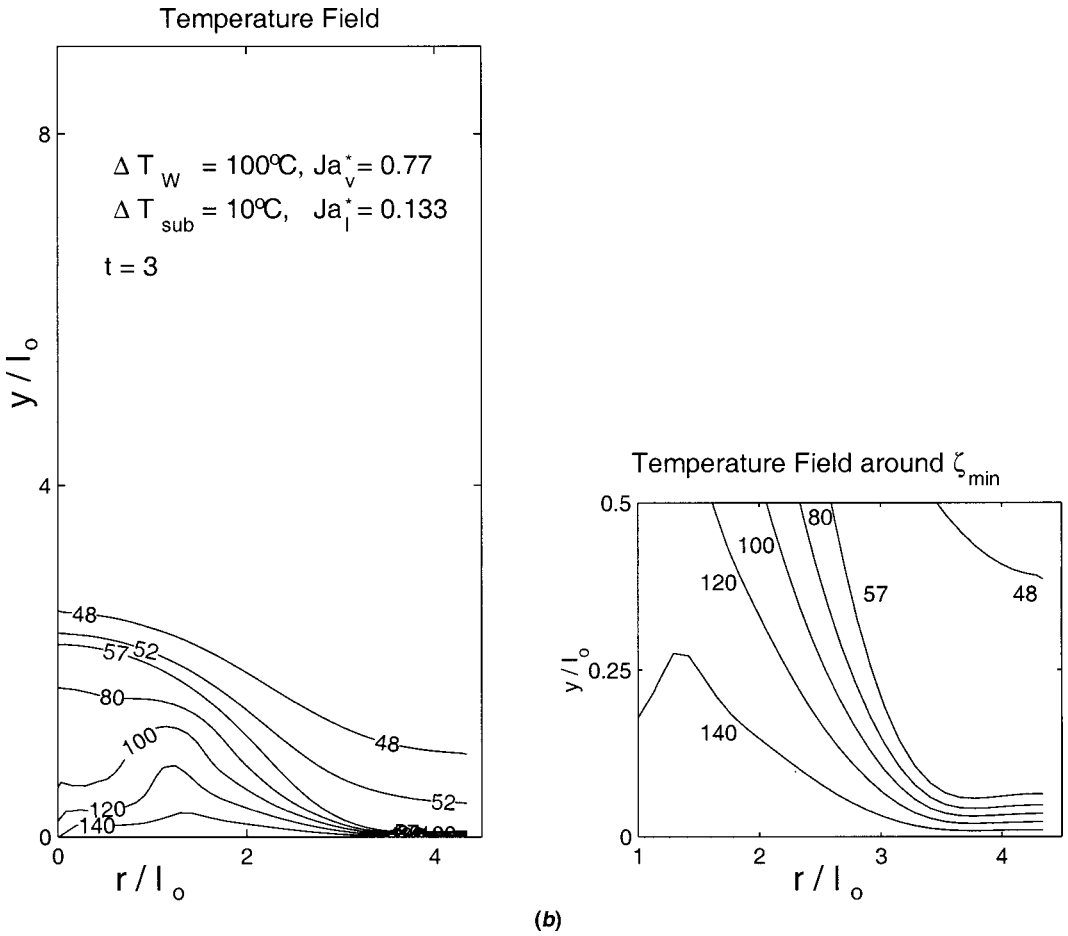

(*b*)

Fig. 7 (***Continued***)

corresponds to k_{n_d}. Hence, no arrows originate from $m=5$ in the second column. When $m=6$ and $n=2$ the only possible value of m for $n=3$ is 12, according to Eq. (60). Hence an arrow has been drawn from 6 in the second column pointing to 12 in the third column in Fig. 1. The possible values of m for succeeding values of n have been listed in the figure, in the columns that follow. A set of arrows are drawn in Fig. 1 to depict the relations akin to those mentioned above. Solution of Eq. (61) yields similar relationships which are also shown in Fig. 1.

From Fig. 1 the most probable solution corresponding to Eq. (60) is found as:

$n=1$	$n=2$	$n=3$	$n=4$	$n=5$
4 or **5**	**8**	**15**	**21**	**27** ’

whereas corresponding to Eq. (61) it is:

$n=1$	$n=2$	$n=3$	$n=4$	$n=5$
4	**9**	**15**	**21**	**27** .

Thus the two formulations give nearly identical solutions with small differences in the number of nodes that are accommodated in the inner rings. Figure 2 shows the location of wave crests (small ellipses) on concentric rings (also shown elliptical). The outer ring denoted by the solid line, and depicted as a large ellipse, represents the outer edge of the circular heater. The radius of each ring (the spacing between each ring being equal to the most dangerous wavelength) is obtained from Eqs. (60) and (61). Since in film boiling vapor bubbles are expected to be released alternatively from nodes and antinodes of the Taylor wave during each half of the cycle, in Fig. 2 the antinodes are depicted by crosses. It is interesting to note that starting with the first ring ($n=1$), the dominant wavelength in the radial and azimuthal directions obtained from the three-dimensional analysis is found to be equal to the ‘‘most dangerous’’ wavelength, λ_{d2}, obtained from two-dimensional Cartesian analysis. Table 1 shows the number of wave peaks supported per λ_{d2}^2 area in the region between consecutive rings. It is seen that about one wave peak is expected to exist over an area equal to square of two dimensional Taylor wavelength.

Next question to be answered before proceeding with the numerical simulation of the evolution of the interface is the extent of the computational domain for the axisymmetric analysis, although the process is three dimensional. Son [5] modeled the alternate release of bubbles from the node and antinode during each half of the cycle from an area equal to λ_{d2}^2. He did so by considering two interacting circular regions of area $\lambda_{d2}^2/2$ that surrounded the node and the antinode (locations of bubble release during the first half and the second half of a cycle, respectively). The analysis revealed that the essential physics of the process could still be retained if either of the circular regions surrounding the node or the antinode was considered and a condition of symmetry was imposed at the outer edge of these areas. The latter approach simplifies the numerical simulations and is utilized here, although the area and time averaged heat transfer coefficients in the latter approach are about 10 percent higher.

3.2 Evolution of the Interface During Subcooled Film Boiling. Figure 3 shows the computational domain used in the present analysis. The dimensionless outer radius, R, of the computational domain has a value of $\sqrt{6\pi}$ or 4.34. The dimensionless height H, of the computational domain was chosen to be 15. Com-

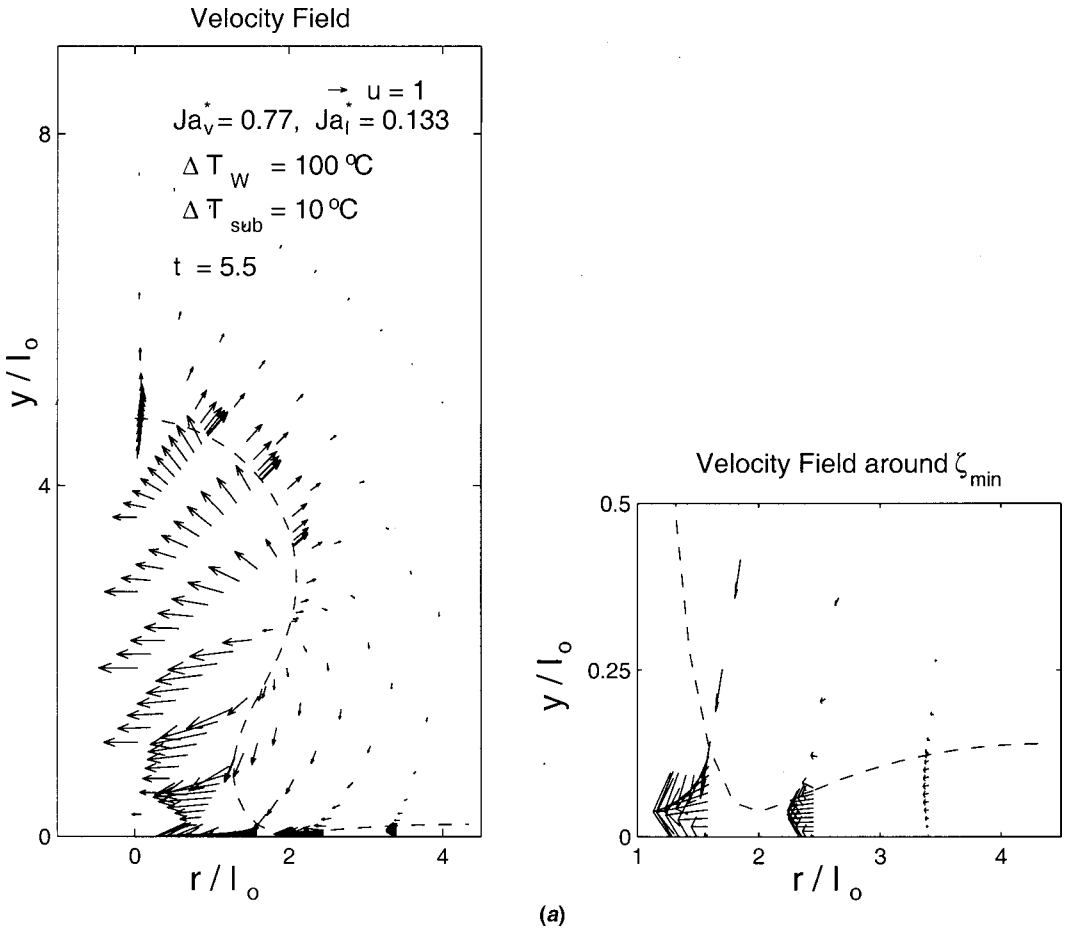

Fig. 8 (*a*) **Spatial distribution of velocity vectors for $\Delta T_W = 100°C$ and $\Delta T_{sub} = 10°C$ at $t = 5.5$. Time is non-dimensionalized with respect to t_o and velocity is non-dimensionalized with respect to u_o. The length of arrows plotted in the figure at the right are 2 times the respective length of arrows in the figure on the left;** (*b*) **spatial distribution of isotherms (θ) for $\Delta T_W = 100°C$ and $\Delta T_{sub} = 10°C$ at $t = 5.5$. Time is non-dimensionalized with respect to t_o.**

putations were performed for thermophysical properties of PF-5060 for wall superheat, $\Delta T_w = 100°C$ and liquid subcoolings ΔT_{sub} of 5°C, 10°C and 22°C. The vapor properties are evaluated at a vapor mean temperature of $(T_{wall} + T_{sat})/2$ and the liquid properties are evaluated at $(T_\infty + T_{sat})/2$. For thermophysical property values of saturated PF-5060 at atmospheric pressure the values of the characteristic length and growth rate are obtained from Eq. (19) as $l_o = 0.735$ mm and $\omega_o = 114.7$ Hz, respectively. Similarly, the characteristic time and velocity obtained from Eq. (38) are $t_o = 8.65$ ms, and $u_o = 0.085$ m/s, respectively.

Initially a vapor film of uniform thickness was perturbed using a Bessel function distribution as follows:

$$\frac{\zeta}{\zeta_0} = [1 + \epsilon J_0(3.832r/R)], \tag{62}$$

where J_o is the Bessel's function of order 0 and a value of 3.832 is the first root satisfying $dJ_o/dr = 0$ (Daly, [11]), and ϵ was set to 0.1. Here ζ is the location of the vapor-liquid interface in the vertical direction from the wall, while ζ_o is the thickness of the undisturbed vapor layer. [Note: ζ_{max} is the maximum height of the vapor liquid interface from the wall and ζ_{min} is the minimum vapor film thickness]. The initial velocity and pressure profiles were obtained from linear stability analysis, as described by Son [5]. Initially a conduction temperature profile (linear) is specified in the vapor region and in the liquid region an error function distribution of temperature is specified. The thickness of the thermal boundary layer in the liquid is derived by assuming that a semi-infinite liquid layer uniformly at subcooled temperature is brought in contact with the interface at the saturation temperature. The duration of contact is assumed to be equal to half of the time period between two consecutive bubble departures at a particular location.

Prediction of Interface Shape and Growth. The evolution of the interface during one cycle was computed. The grid structure at early and late periods of evolution of the interface is shown in Fig. 4. The computations were terminated after the radius of the neck acquired a value smaller than the size of one mesh. In this work, no attempt was made to track the bubble motion into liquid after pinch off. The shapes of the evolving interface at several discrete times from computations for superheat of 100°C and subcooling of 5°C, and 10°C are shown in Fig. 5. The plotted interface height at different radial positions has been non-dimensionalized with the characteristic length. After the outer interface in the middle attains an amplitude of about 3, a ''neck'' starts to form at the base of the evolving interface. After the ''neck'' formation—the interface continues to move inward until the bubble pinches off. The vapor film is thinnest where the interface appears to attach to the heater surface. The location at which minimum film thickness occurs moves radially inward with time. The minimum vapor film thickness is found to decrease with time until just prior to bubble departure, when at the location of minimum vapor film thickness the interface once again moves away from the wall. This is caused by enhanced evaporation due to superheated vapor accelerating at the location of minimum vapor film thickness.

The bubble shapes just prior to departure for the saturated case

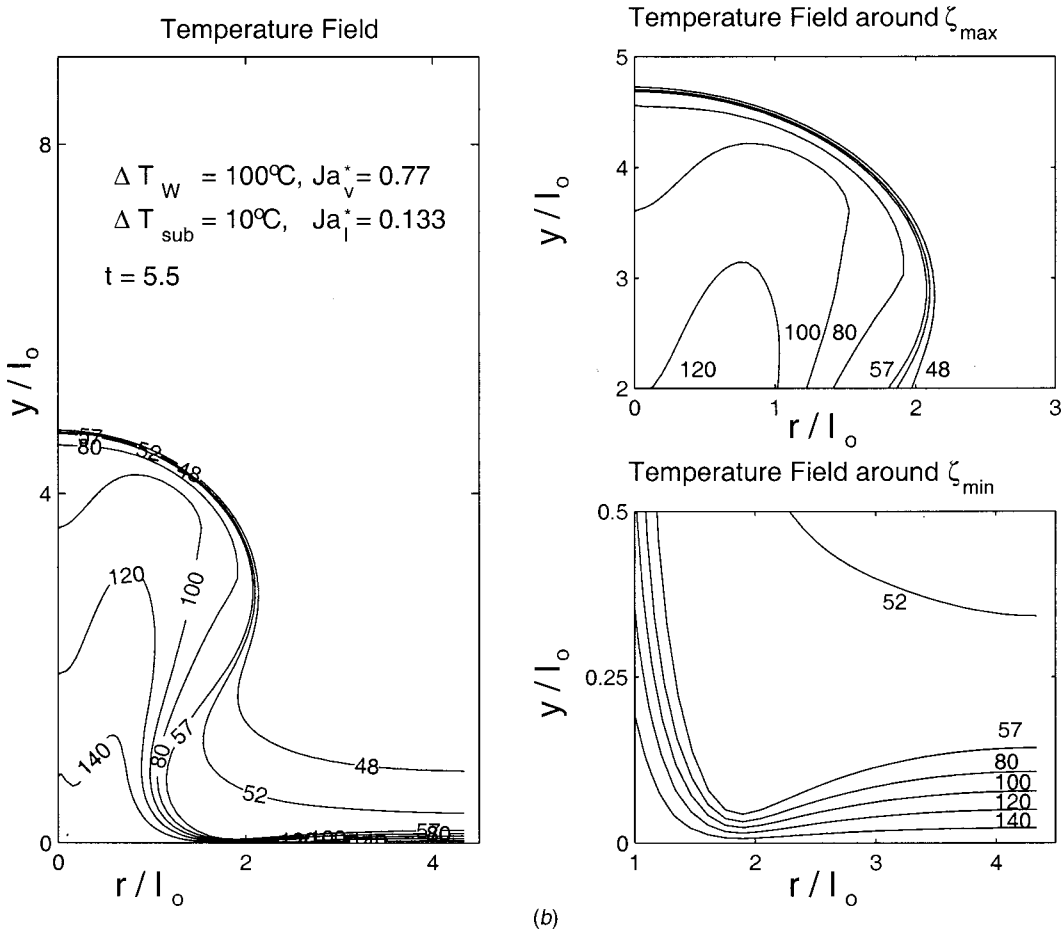

Fig. 8 (***Continued***)

and for subcoolings, $\Delta T_{sub}=5°C$ and 10°C, for a wall superheat of $\Delta T_W=100°C$ are shown in Fig. 6. The effect of liquid subcooling is to reduce the bubble height as well as the sideways growth of the interface. At higher subcooling the liquid drag on the vapor bubble is smaller because of the decrease in growth rate of the interface and correspondingly there is less sideways protrusion of the vapor bubble.

Thermal and Hydrodynamic Analyses. Both vapor and liquid side hydrodynamics significantly modify the heat transfer mechanisms in subcooled film boiling. In Figs. 7 and 8 velocity vectors and isotherms, respectively, have been plotted for a wall superheat of 100°C and for liquid subcooling of 10°C at dimensionless times 3 and 5.5. The figures show that the magnitude of velocities in the vapor phase are much higher than those in the liquid phase. The vapor velocity increases radially inwards in the thin film region because of gradually decreasing flow area as the vapor formed at the interface flows radially inward. The vapor injected into the bubble from the thin film region induces a large convective motion in the bubble. The liquid velocities are higher near the top part of the bubble due to dispacement of the liquid mass by the expanding bubble and diminish in the pool. The radially inward movement of the interface at the neck region causes the liquid from the upper region to flow inward towards the neck region.

The temperature profiles show that the spacing between the isotherms is uniform in the thin film region. This indicates that the energy transfer during film boiling is governed mainly by conduction in the thin film region, rather than by convection. The spacing between isotherms is distorted in the vapor bubble due to large convective motion in the bubble.

It is also observed that the thermal boundary layer is ''squeezed'' at the upper portion of the vapor bubble with rapid evolution of the interface. The thermal boundary layer shrinks as the interface rises at a rate faster than the development of the thermal boundary layer in the liquid. However, the thermal boundary layer in the neck region is quite thick because of lack of upward convective motion.

Heat Flux Partitioning. In contrast to saturated film boiling where liquid side heat transfer is nonexistent, in subcooled film boiling the liquid side heat transfer significantly affects the evapo-

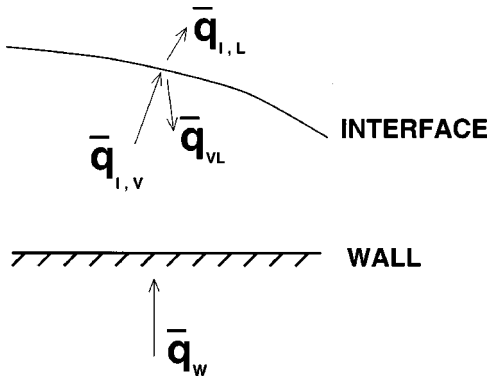

Fig. 9 Schematic of the various heat fluxes at the interface and at the wall in subcooled film boiling

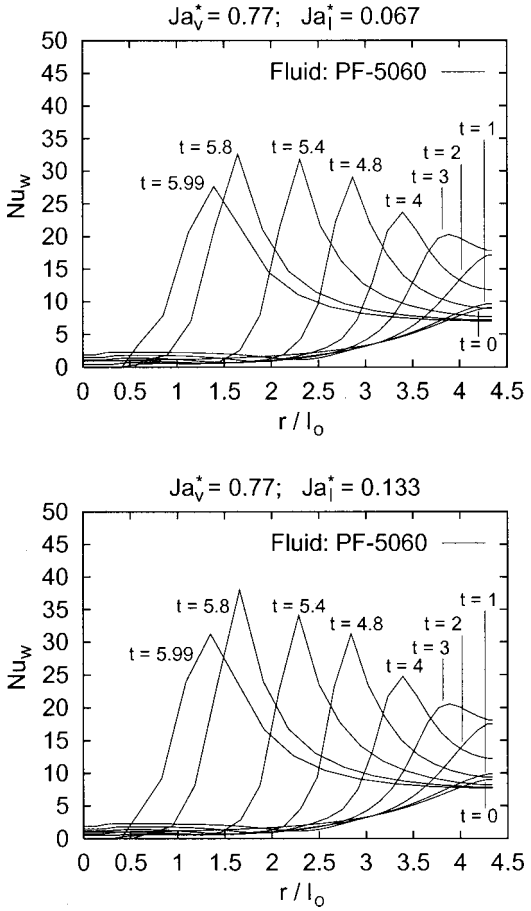

Fig. 10 Plot of temporal variation of local values of wall Nu for wall superheat, ΔT_W=100°C and liquid subcooling, ΔT_{sub} =5°C and 10°C. The radial distances are non-dimensionalized with respect to l_o. Time t is non-dimensionalized with respect to t_o.

ration at the interface and thereby influences the wall heat transfer. Figure 9 shows a schematic representation of the various components of heat flux at the interface. The area averaged heat flux at the wall, $\overline{q_W}$, is partitioned between the sensible heat gained by the vapor (area averaged value), $\overline{q_{VS}}$, and the heat flux at the interface (area averaged) from the vapor side, $\overline{q_{I,V}}$. (The values

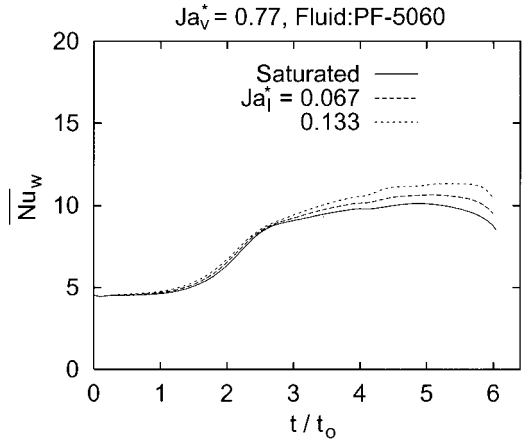

Fig. 11 Temporal variation of area averaged Nu at wall for wall superheat, ΔT_W=100°C and liquid subcooling, ΔT_{sub}=0°C, 5°C, and 10°C. Time is non-dimensionalized with respect to t_o.

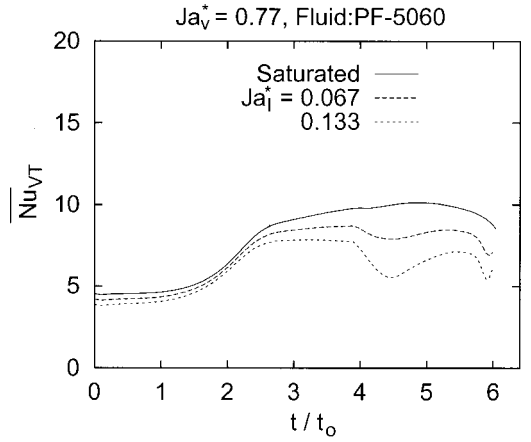

Fig. 12 Temporal variation of area averaged Nu in the vapor phase for wall siperheat, ΔT_W=100°C and liquid subcooling, ΔT_{sub}=0°C, 5°C, and 10°C. Time is non-dimensionalized with respect to t_o.

are averaged over an area bounded by a circle of radius R', where $R'=\lambda_{d2}/\sqrt{2\pi}$.) The area averaged heat flux at the interface from the vapor side $\overline{q_{I,V}}$, is partitioned between area averaged value of heat lost to the liquid at the interface, $\overline{q_{I,L}}$, and the heat flux, $\overline{q_{VL}}$, utilized for vapor production at the interface. Hence the total heat input, $\overline{q_{VT}}$, to the vapor phase as latent heat and sensible heat per unit cell area per unit time, is obtained by summing of $\overline{q_{VS}}$ and $\overline{q_{VL}}$, or

$$\overline{q_W}=\overline{q_{VS}}+\overline{q_{I,V}} \tag{63}$$

$$\overline{q_{I,V}}=\overline{q_{I,L}}+\overline{q_{VL}} \tag{64}$$

$$\overline{q_{VT}}=\overline{q_{VL}}+\overline{q_{VS}}. \tag{65}$$

The above components can be evaluated from the following relationships:

$$\overline{q_W}=\frac{\Delta T_w}{R'^2}\int_{r=0}^{r=R'}-\kappa_v\left(\frac{\partial\theta_v}{\partial y}\right)_{y=0}2rdr \tag{66}$$

$$\overline{q_{I,V}}=\frac{\Delta T_w}{R'^2}\int_{r=0}^{r=R'}-\kappa_v\hat{\mathbf{j}}\cdot\left(\frac{\partial\theta_v}{\partial\hat{\mathbf{n}}}\right)_{y=\eta_0}2rdr \tag{67}$$

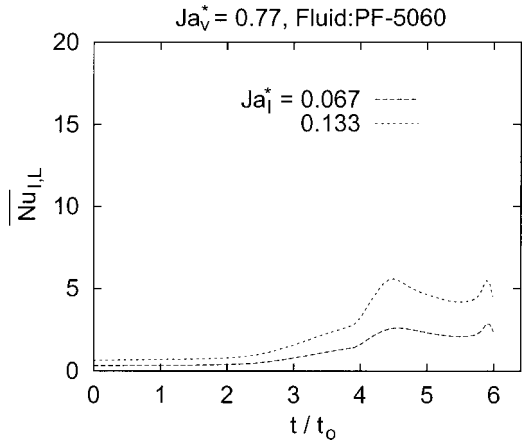

Fig. 13 Temporal variation of component of averaged Nu in the liquid phase for wall superheat, ΔT_W=100°C and liquid subcooling, ΔT_{sub}=5°C and 10°C. Time is non-dimensionalized with respect to t_o.

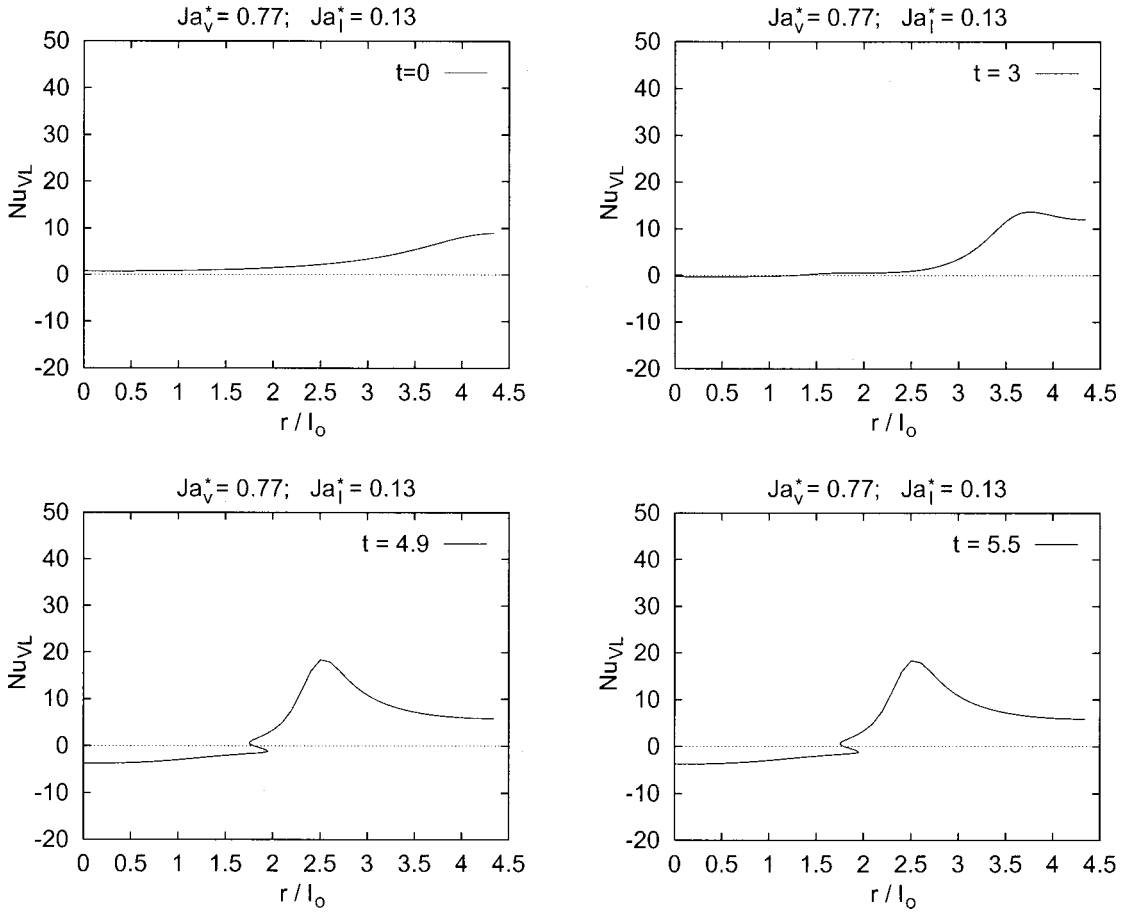

Fig. 14 Plot of local Nu at interface for production of vapor entering the film for $t=0$, 3, 4.9, and 5.5. Time is non-dimensionalized with respect to t_o and radial distance is non-dimensionalized with respect to l_o.

$$\overline{q_{I,L}} = \frac{\Delta T_{\text{sub}}}{R'^2} \int_{r=0}^{r=R'} -\kappa_l \hat{\mathbf{j}} \cdot \left(\frac{\partial \theta_l}{\partial \hat{\mathbf{n}}} \right)_{u=n_0} 2rdr \tag{68}$$

$$\overline{q_{V,L}} = \overline{\dot{m}} h_{fg} \tag{69}$$

where

$$\overline{\dot{m}} = \frac{\rho_v u_0}{R'^2} \int_{r=0}^{r=R'} \dot{m} 2rdr, \tag{70}$$

where $\dot{m}$ is defined in Eq. (51), $\hat{\mathbf{n}}$ is the unit normal vector at any radial location on the interface and $\hat{\mathbf{j}}$ is the unit vector in the y direction. (In saturated film boiling $\overline{q_{I,L}}=0$, and, hence, $\overline{q_{I,V}}=\overline{q_{VL}}$).

The Nusselt number based on area averaged wall heat flux is written as

$$\overline{\text{Nu}_W} = \frac{\overline{q_W} l_0}{\kappa_v \Delta T_W} = \frac{1}{R'^2} \int_{r=0}^{r=R'} \text{Nu}_W 2rdr. \tag{71}$$

Similar Nu can be defined for $\overline{q_{I,L}}$, $\overline{q_{VT}}$, and $\overline{q_{VL}}$ as

$$\overline{\text{Nu}_{VT}} = \frac{\overline{q_{VT}} l_0}{\kappa_v \Delta T_W} \tag{72}$$

$$\overline{\text{Nu}_{I,L}} = \frac{\overline{q_{I,L}} l_0}{\kappa_v \Delta T_W} \tag{73}$$

$$\overline{\text{Nu}_{VL}} = \frac{\overline{q_{VL}} l_0}{\kappa_v \Delta T_W}. \tag{74}$$

Table 2 Predictions for $\overline{\overline{\text{Nu}_W}}$ for $\Delta T_W = 100°\text{C}$

$(\Delta T)_{sub}$ (°C)	Ja_l^*	Numerical Prediction
0	0	7.84
5	0.067	8.12
10	0.133	8.45
22	0.293	8.91

The spatial variation of Nu_W at different times during the evolution of the interface is shown in Fig. 10. Large variations in Nu_W are seen to occur both spatially and temporally. The peak in Nu_W occurs at a point where the vapor film thickness is minimum. The location at which maximum heat transfer (or Nu_W) occurs is seen to move radially inward towards the center with time. Also, the magnitude of maximum heat transfer (or maximum value of Nu_W) increases with time, until prior to bubble departure. Just before bubble departure, the peak value of Nu_W is found to decrease. This result is different from that observed for results from computations when property values of water are used [5]. The value of Ja_v for a wall superheat of 100 °C for PF-5060 is 0.77, and 0.09 for water.

High values of Ja_v imply that liquid can be readily evaporated when exposed to superheated vapor. It is postulated that increase

in the minimum vapor thickness just prior to bubble departure is a result of evaporation induced by the high velocity vapor leaving the film region.

Figure 11 shows the temporal variation of area averaged Nusselt number (or $\overline{\mathrm{Nu}}_W$) computed for the two values of ΔT_{sub}. It is noted that as the interface evolves a significant increase in $\overline{\mathrm{Nu}}_W$ occurs from the initial value. The increase results from the increase in local value of heat transfer coefficient in the thin film region. With increase in liquid subcooling the area averaged heat transfer coefficient increases. However, most of this enhancement occurs in late stages of the evolution of the interface. In order to understand the physics of the process further, we plot in Fig. 12, area averaged Nusselt number based on heat input into the vapor (phase change and sensible heat). It is seen that with increase in liquid subcooling less amount of energy partitions into the vapor. The largest reduction in heat input into vapor occurs when the interfacial area of the evolving interface increase very rapidly. However, subsequently in the later stages of the evolution of the interface some recovery in the total heat input in vapor takes place.

Nusselt number based on area average heat transfer into the subcooled liquid (or $\overline{\mathrm{Nu}}_{I,L}$) is plotted in Fig. 13 as a function of time during the growth period of the interface. At a given time the Nusselt number increases as liquid subcooling is increased. For a given subcooling the Nusselt number remains fairly constant during the initial period but increases very rapidly in the dimensionless time interval between 4 and 5. This is the period during which a rapid reduction in $\overline{\mathrm{Nu}}_{VT}$ was observed. During the bubble growth period as much as five fold variation in liquid side heat transfer is observed. Isotherms in the liquid show that during the period of rapid increase in interfacial area the thermal boundary layer in the upper portion of the bubble thins and in turn leads to an increase in the rate of heat transfer into liquid. However, in the later stages, as the interface slows down, the boundary layer thickens once again and leads to reduced rate of heat transfer into liquid.

In Fig. 14 the Nusselt number based on the energy utilized in producing vapor at the interface is plotted as a function of radial position at different times during the evolution of the interface. It is seen that later periods of the evolution of the interface, negative values of the of the Nusselt number occur at the top portion of the vapor-liquid interface. The negative values imply that heat flux into liquid in the thin thermal layer region is supported by condensation of vapor. At a radial position of about 2, $\overline{\mathrm{Nu}}_{VL}$ is shown to be multi-valued. This is reflection of the shape of the interface and simultaneous evaporation and condensation that occur on different parts of the interface. The maximum value of $\overline{\mathrm{Nu}}_{VL}$ occurs at the location where film is the thinnest.

The calculated values of $\overline{\overline{\mathrm{Nu}}_W}$ based on area and time average heat transfer coefficient at the wall are given in Table 2. As would be expected $\overline{\overline{\mathrm{Nu}}_W}$ increases with increase in Ja_l or liquid subcooling. The enhancement in $\overline{\overline{\mathrm{Nu}}_W}$ results from the fact that wall has to supply not only the energy transferred into the vapor but also into the liquid overlying the thin film region. For the limited range of subcoolings studied in this work, the values listed in the table are correlated as

$$\overline{\overline{\mathrm{Nu}}_W} = \overline{\overline{\mathrm{Nu}}_{W_0}}(1 + 0.5\ \ J^*_{a_l}), \tag{75}$$

where $\overline{\overline{\mathrm{Nu}}_{Wa}}$ is the Nusselt number obtained from the analysis when liquid is saturated. The numerical constant found in Eq. (75) is dependent on wall superheat or $J^*_{a_v}$. The constant will increase nonlinearly as $J^*_{a_v}$ is reduced. For the results presented in Table 2, $J^*_{a_v}$ is 0.77. This value is much higher than that obtained by Dhir and Purohit [17] in their experiments of subcooled film boiling of water. However, Dhir and Purohit's analysis clearly showed a reduction in the constant multiplying $J^*_{a_l}$ as wall superheat was increased. The value of 0.5 obtained in the present work is consistent with that deduced from the results of Dhir and Purohit for high wall superheats.

4 Conclusions

1 Three dimensional Taylor instability analysis in an axisymmetric geometry has been performed. The analysis reveals that most dominant Taylor wavelength during film boiling on a disc is the same as that obtained from 2-D analysis in Cartesian coordinates.

2 Numerical simulation of evolving interface during subcooled film boiling have been performed. The analysis provides the shape and the growth rates of the interface as well as the associated hydrodynamic and thermal behavior.

3 The effect of liquid subcooling is to increase the wall heat flux, mainly because of the heat loss to liquid that occurs in the thin film region. With increased heat loss to the liquid the film becomes thinner.

4 Condensation of vapor occurs on the top portion of the evolving interface whereas evaporation occurs in the thin film region.

Nomenclature

c = constant
c_{pl} = liquid specific heat
c_{pv} = vapor specific heat
g = gravitational acceleration
h = heat transfer coefficient
h_{fg} = latent heat of vaporization
J = Bessel function
Ja* = modified Jacob number
k = wave number
l_o = characteristic length
m = eigen value
n = eigen value
Nu = Nusselt number
p = pressure
Pr = Prandtl number
q = heat flux
R = radius
r = radial coordinate
Ra = Rayleigh number
Re = Reynolds number
R_s = radius of curvature of the interface
t = time
u = radial velocity
v = velocity in the vertical direction
w = velocity in the azimuthal direction
x = coordinate in the horizontal plane
y = vertical coordinate
z = coordinate in the horizontal plane
α = dimensionless wave number
γ = interfacial tension
ΔT_{sub} = liquid subcooling
ΔT_w = wall superheat
κ = thermal conductivity
ζ = interface position from the wall
$\overline{\eta}$ = interface displacement from mean film thickness
θ = dimensionless temperature
λ = wavelength
μ = molecular viscosity
ν = kinetic viscosity
ρ = density
σ = normal stress
τ = shear stress
ϕ = potential function
ω_0 = characteristic growth rate

Subscripts

c = critical
d_2 = most dangerous two-dimensional
IL = interface liquid side
IV = interface vapor side
l = liquid
nc = natural convection
v = vapor
VL = latent heat (vapor phase)
VS = sensible heat (vapor phase)
VT = vapor total
W = wall

References

[1] Berenson, P. J., 1961, ''Film Boiling Heat Transfer From Horizontal Surface,'' ASME J. Heat Transfer, **83**, pp. 351–362.
[2] Hosler, E. R., and Westwater, J. W., 1962, ''Film Boiling on a Horizontal Plate,'' ARS J., **32**, pp. 553–560.
[3] Ramilison, J. M., and Lienhard, J. H., 1987, ''Transition Boiling Heat Transfer and the Film Transition Regime,'' ASME J. Heat Transfer, **102**, pp. 746–752.
[4] Klimenko, V. V., and Shelepen, A. G., 1982, ''Film Boiling On a Horizontal Plate-A Supplementary Communication,'' Int. J. Heat Mass Transf., **25**, pp. 1611–1613.
[5] Son, G., 1996, ''Numerical Simulation of Nonlinear Taylor Instability with Applications to Film Boiling, Melting and Sublimation,'' Ph.D. thesis, University of California, Los Angeles, CA.
[6] Hamill, T. D., and Baumeister, K. J. 1969, ''Effect of Subcooling and Radiation on Film-Boiling Heat Transfer from a Flat Plate,'' NASA TND D-3925.
[7] Dhir, V. K., and Lienhard, J. J., 1973, ''Taylor Stability of Viscous Fluids With Application to Film Boiling,'' Int. J. Heat Mass Transf., **16–11**, pp. 2097–2109.
[8] Bellman, R., and Pennington, R. H., 1954, ''Effects of Surface Tension and Viscosity on Taylor Instability,'' Q. Appl. Math., **12**, pp. 151–161.
[9] Sernas, V., Lienhard, J. H., and Dhir, V. K., 1973, ''The Taylor Wave Configuration During Film Boiling From a Flat Plate,'' Int. J. Heat Mass Transf., **16**, pp. 1820–21.
[10] Jacobs, J. W., 1986, ''Three Dimensional Rayleigh Taylor Instability,'' Ph.D. thesis, University of California, Los Angeles, CA.
[11] Daly, B. J., 1969, ''Numerical Study of the Effect of Surface Tension on Interface Instability,'' Phys. Fluids, **20**, No. 4.
[12] Thompson, J. F., Warsi, Z. U. A., and Mastin, C. W., 1985, *Numerical Grid Generation, Foundations and Applications*, Elsevier Science, North Holland.
[13] Shyy, W., 1994, *Computational Modeling for Fluid Fow and Interfacial Transfer*, Elsevier, NY.
[14] Streett, C. L., and Hussaini, M. Y., 1987, ''Finite Length Effects on Taylor Couette Flow,'' in Stability of Time-Dependent and Spatially Varying Flows, D. L. Dwoyer, and M. Y. Hussaini, eds., Springer-Verlag, New York.
[15] Banerjee, D., 1999, ''Numerical and Experimental Investigation of Subcooled Film Boiling on a Horizontal Plate,'' Ph.D. thesis, University of California, Los Angeles, CA.
[16] Son, G., and Dhir, V. K., 1997, ''Numerical Simulation of Saturated Film Boiling on a Horizontal Surface,'' ASME J. Heat Transfer, **119**, pp. 525–533.
[17] Dhir, V. K., and Purohit, G. P., 1978, ''Subcooled Film-Boiling Heat Transfer From Spheres,'' Nucl. Eng. Des., **47**, No. 1, pp. 49–66.